CO2 sequestration and simultaneous zeolite production by carbonation of coal fly ash: Impact on the trapping of toxic elements

Luis Monasterio-Guillot, Pedro Alvarez-Lloret, Aurelia Ibañez-Velasco, Alejandro Fernandez-Martinez, Encarnación Ruiz-Agudo, Carlos Rodriguez-Navarro

CO_2 sequestration with simultaneous zeolite production and toxic elements trapping by carbonation of Coal Fly Ash

Monasterio-Guillot, L.[1*], Alvarez-Lloret, P.[2]. Ibañez-Velasco, A.[1], Fernandez-Martinez, A.[3], Ruiz-Agudo, E.[1] and Rodriguez-Navarro, C.[1]

1 Department of Mineralogy and Petrology, Univ. of Granada, , 18071, Granada, Spain

2 Department of Geology, Univ. of Oviedo, 33005, Oviedo, Spain

3 Univ. Grenoble Alpes, Univ. Savoie Mont Blanc, CNRS, IRD, IFSTTAR, ISTerre, 38000 Grenoble, France

*corresponding author: luismonasterio@ugr.es

ABSTRACT

Coal-fired power plants are main contributors to atmospheric CO_2 emissions. They also produce huge amounts of coal fly ash (CFA) waste, which is typically landfilled, posing significant environmental risks due to its high content of potentially toxic elements (PTE). However, CFA is an alkaline aluminosilicate-rich waste, which offers the possibility of CO_2 mineral capture and the production of economically-relevant mineral by-products such as zeolites. Yet, the combined carbonation and zeolite production from CFA resulting in PTE trapping has never been explored. Here we show that under mild hydrothermal conditions (150 °C) and depending of process parameters such as pH and background alkali metal ion in alkaline (bi)carbonate solutions, a carbonation efficiency of up to 79%, with a net CO_2 mineral capture of 0.045 g/kg CFA can be achieved, even when using a low Ca and Mg (3.72 wt% CaO, 1.74 wt% MgO) Class F fly ash. Moreover, amorphous zeolitic precursors and different crystalline zeolites (yield

up to 60 wt%) are simultaneously obtained, and PTE in CFA are effectively trapped into the newly formed calcite, zeolitic precursors, and zeolite phases. These results have important implications for carbon capture and storage, as well as for the safe reutilization and disposal of CFA waste.

INTRODUCTION

Coal combustion is the second energy source most used worldwide, with a consumption of 1.4 billion tonnes in 2018, 4% higher than the previous year.[1] It accounts for more than 30% of the global yearly anthropogenic CO_2 emissions, being a key contributor to climate warming and the associated changes in the oceans and atmosphere equilibria.[1] Coal firing also produces huge amounts of coal combustion waste products (CCP), which include coal fly ash, CFA (~70 % of CCP),[2] bottom ash, boiler slag, and fluidized bed combustion wastes.[3,4] Global CFA generation was over 700 million tons (Mt) per year in 2012[3,4], and this figure kept growing in recent years[5]. Management of the huge amounts of CFA waste produced globally is a significant problem, with important economic, health, and environmental implications.[4] Worldwide, ~70% of CFA is disposed of in ash ponds or landfills, the rest being recycled for several applications.[3] Only in the U.S., 34 Mt of CFA were generated in 2016,[1,6] of which 20 Mt were used mainly as a construction material due to its pozzolanic properties (e.g., concrete products, blended cements, road base) or in mining applications; still, 14 Mt of CFA were discarded and subjected to ponding or landfilling.[7] In addition to the huge area needed to store or dispose of CFA,[8] this waste includes a significant amount of potentially toxic trace elements (PTE)[9–11] which may

limit its recycling capability and make CFA spilling or leaching a hazard resulting in contamination of soils, water bodies and groundwater.[12–16]

Reutilization processes for CFA waste other than its use in construction include: (i) synthesis of zeolites[17–19], which are microporous crystalline aluminosilicates formed by corner-sharing tetrahedral groups conforming voids and channels that allow the adsorption of gases, metal ions and organic molecules.[9,18,20–22] Due to their pore characteristics and high ion exchange capacity,[23] CFA-derived zeolites are employed for CO_2 (and other pollutant gases) capture, removal of toxic metals, water decontamination, and soil improvement.[18,19,24–26] CFA-derived zeolite synthesis has focused on the use of NaOH (and KOH) for hydrothermal, alkali fusion, or microwave-assisted production.[19] A few works explored the use of alkali carbonate activators for hydrothermal zeolite synthesis (120 °C), reporting a limited zeolite yield but, interestingly, resulting in calcium carbonate precipitation.[20] The latter suggests that the combined carbonation and zeolite synthesis using CFA is feasible. Although several works have shown that zeolites formed after CFA can be used to capture PTE[18,19], no study has evaluated the actual trapping of PTE present in the CFA used for zeolite synthesis; and (ii) to a lesser extent, CFA has been used for carbon capture and storage (CCS) via accelerated mineral carbonation.[27–33] Despite the limited foreseen contribution of CFA to mineral carbon sequestration (~7.6 $Mt/CO_2/y$),[34] its use for carbon capture, utilization and storage (CCUS) must be considered as it could contribute to the reduction of the C footprint of coal-fired power plants,[1,6,30] result in the production of economically-valuable by-products such as carbonates and zeolites, and in a reduction of the

potential leaching of PTE during CFA disposal.[30] Previous works have evaluated the carbonation efficiency (CE) and net CO_2 capture of CFA from different sources and compositions under a range of process conditions (e.g., direct and indirect carbonation, dry vs. wet processes, pH, *T*, solid/solution ratios, aqueous solution composition, pCO_2).[3,35] These studies show that CE values are typically <<80% [5,36], and the net CO_2 capture can be as low as ~8 kg per ton of CFA. With a few exceptions (CFA with CaO + MgO > 20 wt%[2,11,33]), the average CaO content in CFA is 7±3 wt%,[35] resulting in relatively low values of effective CO_2 mineral capture. The limited CE and relatively low net CO_2 capture capacity have been strong handicaps for the widespread implementation of CCS strategies for CFA. In spite of some efforts to improve CE values,[5,37] progress in this direction has been limited, mostly because the mechanisms of CFA carbonation are not fully understood. For instance it has been assumed that only the easily leached crystalline phases containing calcium (e.g., CaO and $Ca(OH)_2$) were able to feed the solution for CFA carbonation.[30,33] However, a significant fraction (≥50%) of CaO (and MgO, which can also contribute to CO_2 mineralization) in CFA is present in the not-so-easily leachable amorphous aluminosilicate phase, which typically accounts for ≥70 wt% of CFA.[11] It is thus necessary to better understand the carbonation mechanisms of CFA and to explore means to effectively leach the Ca and Mg present in such amorphous phase in order to achieve the highest possible CE. Moreover, no work has evaluated the potential of CFA carbonation as a means to achieving an effective CCUS by the simultaneous production of valuable zeolite by-products, while trapping PTE.

The aim of the present work is to experimentally disclose the key features of CFA carbonation under mild hydrothermal conditions using alkaline (bi)carbonate solutions, combined with the formation of zeolites and the effective capture of PTE present in CFA.

MATERIALS AND METHODS

Characterization of unreacted Coal Fly Ash and reaction products. CFA used in this study was provided by the Compostilla thermal power plant in León (Spain). The concentrations of major/minor and trace elements in unreacted CFA were determined on a Bruker AXS S4 Pioneer X-ray fluorescence (XRF) equipment. Identification and quantification of mineral phases in unreacted CFA and solid products collected after carbonation experiments (see below) was performed by powder X-ray diffraction (XRD), using a X'Pert PRO diffractometer (PANalytical) with the following instrumental parameters: Cu-Kα radiation, Ni filter, 40 mA current, 45 kV tension, 3-70 °2θ exploration range, 0.004 °2θ step size, and 29.84 s per step. The HighScore Plus 2.2.4 software (PANalytical) was used to process the XRD patterns and to identify mineral phases by matching the experimental diffraction patterns to those included in the PDF-2 database.[38] Quantitative mineralogical analysis was performed by Rietveld analysis[39] using the Internal Reference Method[40] (5 wt% crystalline Si powder added as internal standard) and the crystal structures provided by the American Mineralogist Crystal Structure Database (Supplementary Material Table S1). Solids were also analysed by Fourier transform infrared spectroscopy (FTIR) with an attenuated total reflectance (ATR) sample holder (Jasco 6200 FTIR) in the frequency range 400–4000 cm^{-1}, with a spectral resolution of 2 cm^{-1}, step size of

0.48 cm^{-1} and 126 accumulations. Thermogravimetric analyses, TGA (TGA-DSC3+, Mettler Toledo) were performed under flowing N_2 using a linear heating rate of 20 ºC min^{-1}, from 30 to 950 ºC. Reactant CFA and solid products were also analyzed by field emission scanning electron microscopy (FESEM, Auriga Carl Zeiss SMT) equipped with energy dispersive X-ray spectroscopy (EDS). Prior to analysis, solids were carbon coated. Further ultrastructural and compositional details of reactant and product phases were studied by means of transmission electron microscopy (TEM) on a FEI TITAN at 300 kV acceleration voltage, and equipped with a high angle annular dark field detector (HAADF) for Z-contrast imaging. Analytical electron microscopy (AEM) was performed by EDS microanalysis (under scanning-TEM operation mode) using the thin-foil method[41] and *k*-factors determined using standard minerals of known composition. Once each carbonation run was completed, the concentration of selected ions in solution after filtration was determined by ICP-OES (Perkin Elmer, Optima 8300 or Varian 720ES). Finally, N_2 sorption isotherms of unreacted CFA and carbonation products were performed at 77 K on a TriStar 3000 equipment (Micromeritic), after sample degassing at 150 °C for 12 h under vacuum (0.07 torr) in a Flow Prep device (Micromeritics).

CFA carbonation experiments. To disclose the effect of pH and background electrolyte on carbon capture and zeolite synthesis efficiency, direct carbonation experiments in aqueous solution were performed under hydrothermal conditions (150 ºC):[33] (i) without dissolved inorganic carbon (DIC) (control, A-experiments), and (ii) with dissolved sodium or potassium (bi)carbonate (N-, and K-experiments, respectively). Table 1 shows details of the different

experimental runs. A *T* of 150 °C was selected to favour the dissolution of mullite and quartz present in the unreacted material.[42] 0.0043 mol mL^{-1} Na_2CO_3, $NaHCO_3$, K_2CO_3 and $KHCO_3$ solutions were prepared using ultrapure MilliQ water (resistivity 18.2 MΩ·cm, Millipore) and >97%-grade solid reactants from Sigma-Aldrich. A relatively high reactant concentration was selected in order to ensure an excess of carbonate and to achieve a range of pH values from ~8 up to ~12. In a previous work we showed that a similar alkali (bi)carbonate reactant concentration was optimal for the carbonation of pseudowollastonite ($CaSiO_3$).[43] Note that such alkali metal (bi)carbonate solutions are a proxy for alkali metal hydroxide solutions in which CO_2 gas is dissolved, and the solutions can be regenerated via CO_2 injection,[5] which could be the actual protocol for implementing *ex situ* carbonation involving CO_2 capture at emission point sources. 1 mL of the solutions was added to 500 mg of CFA in a PTFE vessel (polytetrafluoroethylene, 3 mL total volume). Afterwards, the PTFE vessel was inserted into a steel reactor designed for high *T*-*P* conditions. After sealing, the reactors were heated to 150 °C for 72 h (longer runs for up to 7 days showed no additional changes in the progress of the reaction). Then, the autoclaves were cooled down to room *T* and opened. The content of the vessels was immediately filtered (0.2 μm membrane filter, Millipore) and the solids were oven-dried for 24 h at 60ºC. The pH of the solutions before and after the experiments was measured at room *T* using a glass electrode (Metrohm) calibrated with three standard solutions (pH= 4.01, 7.01 and 10.01 at 25 °C) with ±0.01 uncertainty. In order to ensure statistical representativity, all runs were performed in triplicate.

Calculation of Carbonation Efficiency (CE). We considered that all amorphous and crystalline Ca- and Mg-containing phases (excluding already formed $CaCO_3$) in unreacted CFA can contribute to the leaching of Ca and Mg in solution and therefore, to the effective carbonation of CFA.[35,44] Multiple equations have been proposed to calculate the CE for CO_2 sequestration.[5,28,30,37,45,46] In this study, we calculated the CaO contained in the calcite present in unreacted CFA using eq. 1:

$$iCaO = wt_{CaCO3}\, x \frac{M_{CaO}}{M_{CaCO3}} = 0.56\, wt\,\% \quad (1)$$

where wt_{CaCO3} is the wt% of $CaCO_3$ determined by the XRD analysis of the unreacted material using the Rietveld method, M_{CaCO3} is the molar mass of $CaCO_3$ (100 g mol^{-1}) and M_{CaO} is the molar mass of CaO (56 g mol^{-1}). $iCaO$ is subtracted from the total CaO + MgO content of the unreacted material, to determine the theoretical sequestration capacity of our CFA using the Stenoir formula,[28,45,46]

$$Th_{Cc} = \left(wt_{CaO} - iCaO\right) + wt_{MgO} = 4.87\, wt\,\% \quad (2)$$

where wt_{CaO} and wt_{MgO} are the content of CaO and MgO, respectively, in unreacted material measured by XRF. Finally, we adapted the equation used by Dananjayan et al.[28] to calculate CE (%) as follows:

$$CE = \frac{\left[\left(\Delta wt\,\%\, 590\,^{\circ}C - 800\,^{\circ}C\right) \times \left(M_{(Ca,Mg)CO3} / M_{CO2}\right)\right] - 1}{Th\,Cc}\, x\, 100 \quad (3)$$

where $\left(\Delta wt\,\%\, 590\,^{\circ}C - 800\,^{\circ}C\right)$ was calculated from TGA analyses, and $M_{(Ca,Mg)CO3}$ is the molar mass of calcite in the products, which can include a fraction of Mg replacing Ca (i.e., Mg-calcite) (see Results below).

Leaching experiments. Continuous flow-through experiments were performed to evaluate the PTE leaching capacity of both the unreacted and reacted CFA. Leaching experiments were performed at 25 °C using PTFE reactors (V_{tot} = 30 mL; lined with double polycarbonate 0.2 μm filters to prevent solids loss) under constant magnetic stirring. 1 g of solids was placed in each reactor and the experiments started by continuously flowing MilliQ water at a rate of 2 mL min^{-1}. In order to evaluate the effect of pH on PTE leaching, experiments were performed at a near-neutral pH 6 and at an alkaline pH 10 (adjusted using 1M NaOH), the latter corresponding to the natural pH of the studied CFA (Table 1). Aliquots of the effluent solution were collected at predefined time intervals (30 min, 60 min, 90 min, 3 h, 6 h, 9 h and 24 h) and their PTE content was determined by ICP-MS on a NexION 300D equipment.

Code	Solutions	Initial pH	Final pH	Zeolitic content (wt%)	Carbonate content (wt%)	Mg content (mol%)	CE (%)
A1	MilliQ H_2O	9.26	9.8	0	1	0	0
N1	3.4M Na_2CO_3	11.63	10.77	60	4.9	1.19	79.26
N2	3.4M $NaHCO_3$	8.26	9.79	0	3.2	7.74	34.29
K1	3.4M K_2CO_3	12.02	11.35	33	3	1.36	44.96
K2	3.4M $KHCO_3$	8.2	9.32	0	2.6	2.43	33.88

Table 1. Experiment codes, solution composition, initial and final pH, zeolitic content, carbonate content, Mg content in calcite and Carbonation Efficiency (CE) for each experimental run.

RESULTS AND DISCUSSION

Chemistry and mineralogy of unreacted CFA. XRF analysis (Table S2) shows that Si, Al and Fe account for more that 80 wt% (expressed as oxides) of the CFA. Compositionally, this CFA

can be classified as Class F, the most common and abundant type of CFA worldwide[47]. The relatively low CaO plus MgO content (5.43 wt%), which approaches the average alkaline-earth metal oxide content of CFA[35], poses a limit to the maximum net CO_2 capture capacity of this CFA. Several PTE are present in significantly high concentrations (e.g., Ba=1345 ppm; V=849; Cr=189; As=150 ppm), also on the same range of concentrations reported for other CFAs[11,48]. These results underline the potential toxicity of CFA leachates. XRD analysis (Figure 1a) shows that this CFA is composed of a glass fraction (95±2 wt%), graphite (2.0±0.1 wt%), quartz (1.2±0.1 wt%), mullite (1±0.1 wt%), calcite (1±0.1 wt%) and traces of hematite (<1 wt%). The presence of calcite in the unreacted fly ash is likely due to partial hydration of free CaO to $Ca(OH)_2$ and its subsequent carbonation to $CaCO_3$ during sample handling. Due to the low calcite content in this CFA, very low intensity (not easily visible) carbonate bands were detected in FTIR spectra (Figure 1b). FTIR analysis also shows high intensity bands at 1009 cm^{-1} and 650-720 cm^{-1}, corresponding to the asymmetric and symmetric vibration of T-O (T = Si or Al), respectively, and at 400-500 cm^{-1}, corresponding to T-O bending as well as combination modes of the aluminosilicate glass.[49,50] FESEM observations show that the CFA is made up of spheres and cenospheres (and a few plerospheres) with size ≤ 20 μm (Supplementary Material, Fig. S1). TEM-AEM analysis shows that this CFA is mainly composed of amorphous (see diffuse haloes in SAED patterns) micrometer-sized aluminosilicate glass spheres and scarce C-rich aggregates with embedded aluminosilicate spheres (Fig. S2). AEM point analyses (Table S3) yield the following overall composition (wt%) for the spheres (N=6): 50.7±2.5 SiO_2, 32.7±1.8 Al_2O_3,

5.2±1.1 Fe_2O_3, 3.1±1.1 MgO, 2.6±2.5 CaO, 3.8±0.6 K_2O, 1.4±0.2 Na_2O, and 0.6±0.2 TiO_2, values very similar to those of the bulk CFA determined by XRF analysis (Table S2). This is not surprising considering that the glass phase accounts for nearly 95 wt% of CFA. Our AEM results also show that the amorphous spheres include ~70 % and ~100 % of the total CaO and MgO in the CFA, respectively. This underlines that to achieve the highest possible CE, the glass phase has to be fully dissolved. EDS elemental maps show that the spheres include different PTE, and quantitative AEM point analyses (Table S3) yield the following average contents for selected PTE: V= 633 ppm, As= 416 ppm, Mn= 66 ppm; Cr= 16 ppm; Zn= 66 ppm, values consistent with XRF results.

The chemical and mineralogical composition determined for our CFA is in very good agreement with that reported by Moreno et al.[11] for CFA from the same source and, despite the reported variability,[35] is very similar to that of other Class F CFAs.[9,18–23,30,31] We are thus confident that our CFA is representative for Class F CFAs from several coal-fired power plants.

C**arbonation/zeolitization reaction.** XRD patterns of reacted CFA are shown in Figure 1a. Rietveld quantification shows that in Na_2CO_3 (N1) runs, a zeolite yield of ~60 wt% is obtained, which is substantial for hydrothermal CFA-derived zeolite synthesis (typical yields are in the range 20-65%).[51] Analcime (8 ± 2 wt%), Na-chabazite (17 ± 6 wt%), NaP1 zeolite (31 ± 9 wt%), and hydroxysodalite (4 ± 1 wt%) are identified, along with calcite (5 ± 1 wt%), hematite (<1 wt%), quartz (<1 wt%), mullite (<1 wt%) and glass (33 ± 9 wt%). In K_2CO_3 (K1) runs, the dissolution of the glass fraction and the subsequent precipitation of zeolites is more limited. Our

quantitative XRD results show the presence of K-zeolite (33 ± 9 wt%), calcite (3.4 ± 0.8 wt%), hematite (<1 wt%), quartz (<1 wt%), mullite (<1 wt%) and glass (61 ± 14 wt%). XRD analyses show no zeolites, nor any changes in terms of phase composition in N2, K2 and control (A1) runs, as compared with unreacted CFA.

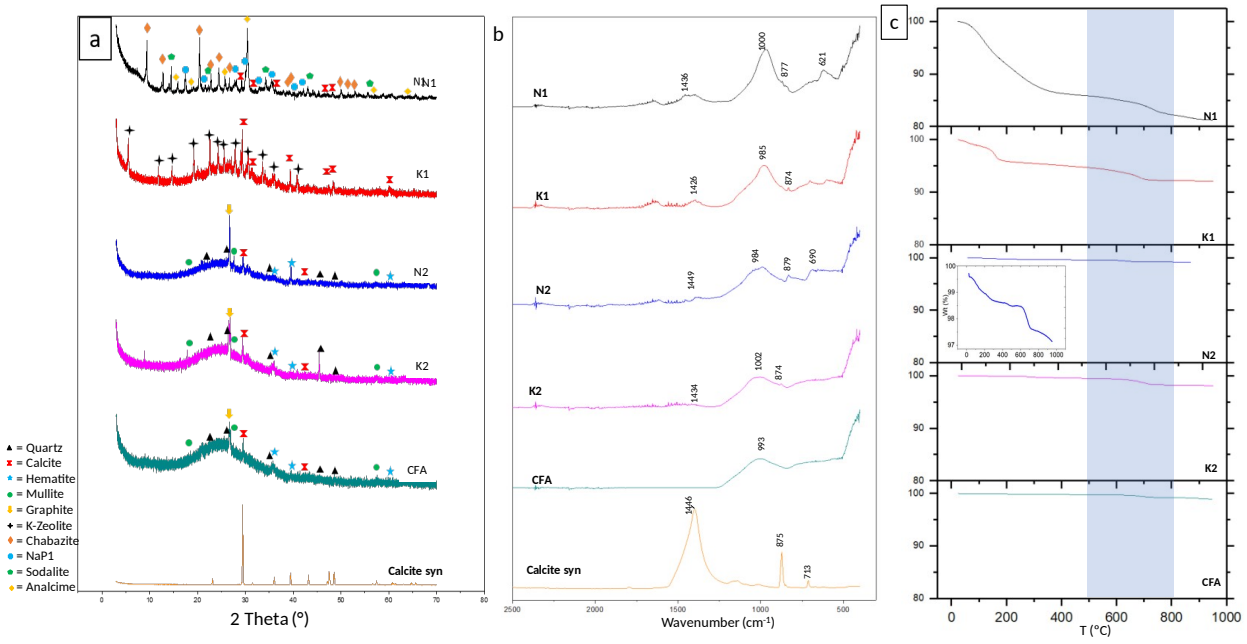

Figure 1. Unreacted CFA and products of its reaction in different carbonate solutions at 150ºC; Na_2CO_3 (N1), K_2CO_3 (K1), $NaHCO_3$ (N2), $KHCO_3$ (K2). (a) XRD patterns showing the Bragg peaks of the different crystalline phases; legend in inset; (b) FTIR spectra; and (c) TGA traces (insets show TGA traces with enlarged Y-axis). The shaded blue area represents the starting and the final *T* of carbonate decomposition (550-800 ºC).

FTIR spectra of samples K2, N2, K1 and N1 show well-defined bands at ~710 cm^{-1}, ~875 cm^{-1} and/or ~1440 cm^{-1} that confirm the new-formation of calcite (Fig. 1b). They also show the broad band at ~1000 cm^{-1} (T-O asymmetric stretching) of aluminosilicate phases. Bands at ~650-870 cm^{-1} corresponding to the T-O symmetric stretching, at ~442-503 cm^{-1} corresponding to the T-O bending, and at 550-575 cm^{-1} corresponding the double rings of

analcime,[52] sodalite, NaP1 zeolite and Na-chabazite,[52] as well as K-zeolite,[53] are observed in runs N1 and K1 respectively. Solids collected after runs N2 and K2 (bicarbonate runs) show similar T-O band as those described above. They also show the broad band at ~1000 cm-1 (T-O asymmetric stretching), and less intense (and poorly resolved) bands at ~650-870 cm-1 (T-O symmetric stretching) and the very intense, broad band at ~400-500 cm-1 corresponding to the T-O bending of aluminosilicate phases, consistent with the presence of unreacted CFA and newly-formed zeolites (in the case of runs N1 and K1) (confirmed by TEM-SAED analysis, see below).[54–56] No changes are detected in the FTIR spectra of the control run (A1) as compared with that of unreacted CFA. In combination with XRD, the FTIR results further demonstrate that a hydrothermal treatment with pure water leads to no mineral or structural changes to CFA.

TG-DSC analyses (Fig. 1c) show that the starting material and all products display a weight loss in the temperature range 550-800ºC, related to the thermal decomposition of calcium carbonate according to the reaction $CaCO_3 = CaO + CO_2$.[57] However, we observe that the starting *T* for the thermal decomposition of carbonates differ among runs, suggesting that either there are changes in calcite particle size (smaller size-fractions decomposing at lower *T* than larger size-fractions) and/or that Mg partially replaces Ca in the calcite phase, forming a (low) Mg-calcite, therefore lowering the starting decomposition temperature.[58,59] Note that XRD analyses show no (crystalline) magnesium carbonates. We performed unit-cell refinement using Rielveld analysis to determine the Mg content in calcite using the method proposed by Goldsmith and Graff (1958)[60] (results in Table 1). Calcite in unreacted CFA has no Mg. The

highest Mg content in newly-formed calcite is observed in N2 runs, followed by K2, K1 and N1 runs. These results are in full agreement with TGA results and with the first derivate of the DSC analyses (Figure S3), showing a lower starting decomposition *T* for the Mg-calcites with the highest Mg content. We suggest that at a moderately alkaline pH (bicarbonate runs), the higher $[Ca^{2+}]/[CO_3^{2-}]$ ratio (closer to unity) as compared to higher pH runs (with higher $[CO_3^{2-}]$) could enable faster calcite growth favoring Mg incorporation.[61] From the weight loss in the *T* range 550-850 °C, CE values of 34%, 34%, 45% and 79% are obtained for K2, N2, K1 and N1 runs, respectively. TGA analyses show an additional weight loss at 105-200ºC in N1, K1, N2 and K2 runs. In the case of N1 and K1 runs, this is likely due to loss of zeolitic water. Conversely, in runs N2 and K2, which lack crystalline zeolites, the weight loss is likely due to the decomposition of residual $NaHCO_3$ and $KHCO_3$ according to the reaction $2MHCO_3 = M_2CO_3 + CO_2 + H_2O$, where M is a monovalent cation (K or Na). However, we cannot rule out the possibility that this weight loss is due to dehydration of an amorphous zeolitic precursor. In any case, it should be noted that Na_2CO_3 and K_2CO_3 (if present as a residual) would undergo melting at 850ºC and 900ºC, respectively, therefore not interfering with the calcium carbonate decomposition, nor releasing any CO_2 at lower *T*.[62] In all runs, including the control and unreacted CFA, the limited initial weight loss at $T < 550$ °C is likely due to dehydration of amorphous silica.[43] Note that such a weight loss overlaps with the weight loss associated with zeolitic water in runs where zeolites (and zeolitic precursors) are formed.

FESEM images show the presence of calcite (as indicated by XRD analysis) in all

carbonation runs (Fig. 2). Calcite appears as micrometer sized rhombohedral crystals attached to CFA spheres (Fig. 2b-c). Reacted CFA spheres have irregular surfaces coated by newly formed precipitates (Fig. 2b-c). It was, however, not possible to clearly differentiate by EDS microanalysis the composition of these precipitates from that of the unreacted spheres. According to Murayama et al.[20] these coatings are most likely composed by new Si-Al phases formed after partial dissolution of the spheres and re-precipitation at the sphere-solution interface. Such newly-formed precipitates could act as a passivation layer on CFA particles, acting in a similar way as the amorphous silica-rich surface layers formed during weathering of primary silicate minerals.[63–66] SEM-EDS analysis corroborates XRD analyses showing the presence of NaP1 (Fig. 2d), Na-chabazite (hershelite) (Fig. 2e), hydroxysodalite/cancrinite, and analcime (Fig. 2f) in N1 run, and K zeolite in K1 run (Fig. 2g).[9,52] SEM-EDS analysis also show that Sr, W and Ce are incorporated into the newly formed carbonates (Fig. S4a-b), V is trapped in zeolite phases, and Cu is incorporated in both newly-formed phases (Fig. S4c-d). Conversely, SEM-EDS analysis of carbonates formed in N2 and K2 experiments shows no trapping of PTE, although we observe the presence of scattered shapeless coatings on some CFA spheres (Fig. 2h), likely corresponding to an amorphous zeolitic precursor,[55] as confirmed by TEM-SAED and AEM analyses (see below). Due to the background signal from the underlying spheres we could not clearly determine using EDS microanalysis whether or not PTE are trapped in these latter precipitates. We argue that the extensive dissolution of the glass particles in N1 and K1 runs favored the release and subsequent trapping of PTE into the newly formed carbonate and zeolite

phases. No trapping of PTE into the limited amount of newly formed crystalline phases (i.e., carbonates) in runs N2 and K2 is detected by SEM-EDS, likely due to the limited dissolution and PTE release from the glass phase Yet it is likely that the newly-formed amorphous zeolitic precursors formed in the bicarbonate runs also trapped PTE (see TEM-AEM results below).

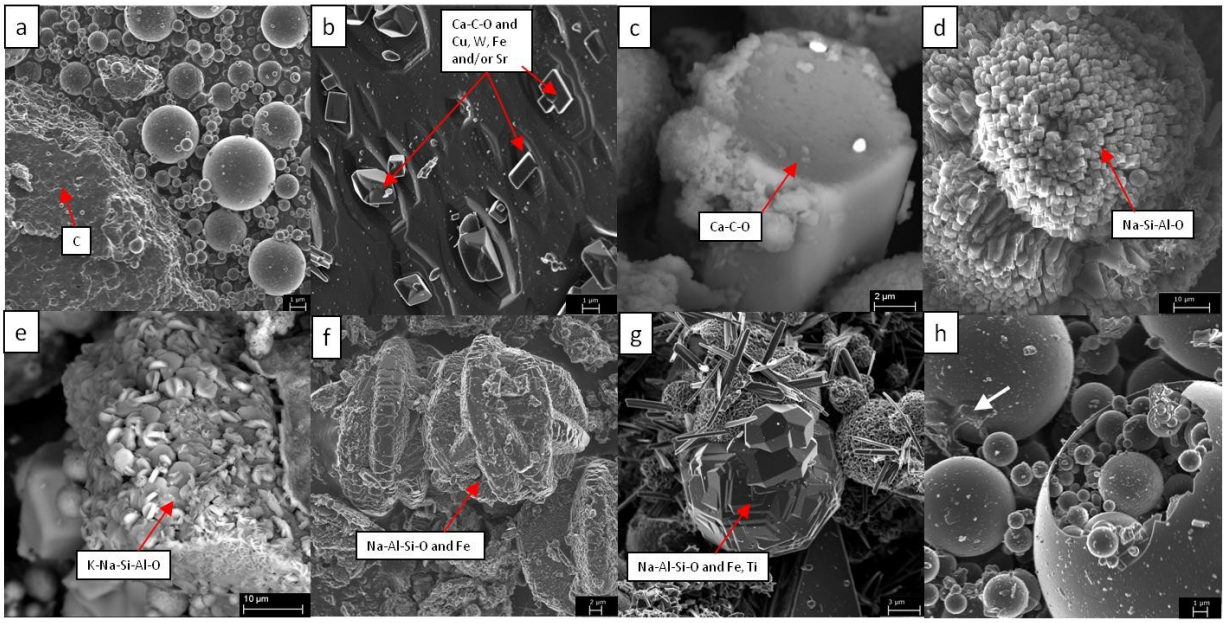

Figure 2. FESEM images of: (a) unreacted spheres of CFA and a graphite (C) particle; (b) calcite in N1; (c) calcite in K1; (d) NaP1 zeolite in N1; (e) K-zeolite in K1; (f) Na-chabazite (hershelite) in N1; (g) analcime in N1; and (h) large plerosphere (lower left) and solid spheres in run N2. The white arrow points to a shapeless deposit with features resembling an amorphous zeolitic precursor. The EDS elemental composition of the red-arrowed particles are shown in the insets.

TEM-AEM analysis of reacted CFA shows significant mineralogical and compositional changes in the case of run N1, i.e., the run with the highest carbonation and zeolitization level (Fig. 3). Aggregates of newly formed poorly crystalline zeolitic nanophase with diffuse Debye rings in the SAED pattern and with d_{hkl} values consistent with a Na-chabazite (precursor) phase are observed (Fig. 3a). In addition, well crystallized Na-chabazite crystals are identified by their

311 SAED pattern (Fig. 3b). HAADF images and corresponding EDS maps confirm the formation

312 Na-zeolites, which include different PTE (Fig. 3c-d).

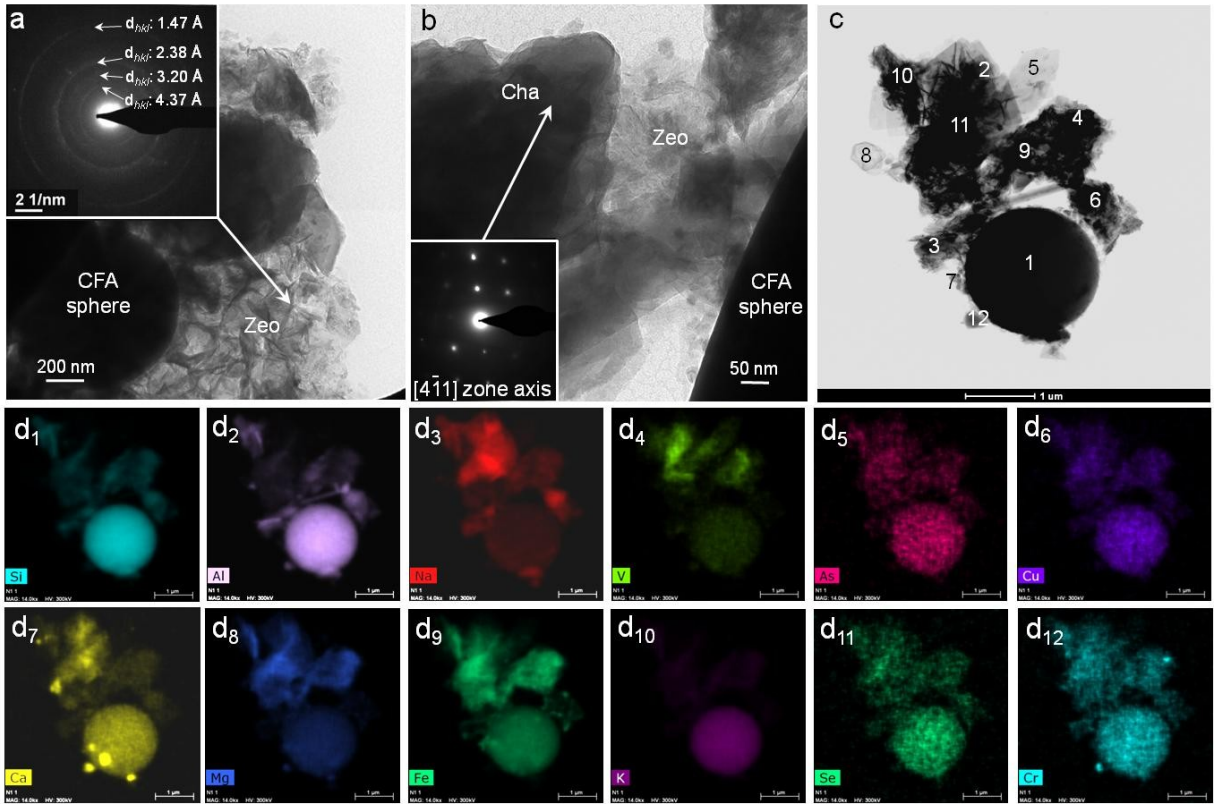

313

314 **Figure 3.** TEM-AEM analysis of reaction products of run N2. (a) Relict CFA sphere and newly

315 formed zeolites (Zeo). The inset shows the SAED of the aggregate at the lower right. The

316 diffuse Debye ring at the indicated d-spacing show the presence of a poorly crystlline precursor

317 phase to Na-chabacite; (b) Large well-crystallized Na-chabazite (its [4-11] zone axis SAED

318 pattern is shown in inset); (c) HAADF image of a sphere surrounded by newly-formed product

319 phase. The numbers indicate AEM point analyses with composition reported in Table S4. (d1-

320 d12) EDS elemental maps of the particles shown in (c).

321

322 Quantitative AEM point analyses (Fig. 3e and Table S4) demonstrate the presence of

323 Na-chabazite with formula $Na_{3.4}K_{0.24}Mg_{0.28}Fe_{0.18}Al_6Si_{5.6}O_{24}\cdot 12H_2O$ (analysis 3 in Table S4), NaP1

324 with formula $Na_{6.32}K_{0.59}Mg_{2.69}Fe_{1.09}Al_{5.19}Si_{10}O_{32}\cdot 12H_2O$ (analysis 10 in Table S), and

hydroxysodalite with formula $Na_{5.53}K_{0.14}Mg_{0.09}Fe_{0.24}Al_{4.71}Si_6O_{24}(OH)_2 \cdot 2H_2O$ (analysis 6 in Table S4) plus a Na-poor aluminosilicate phase with a Si/Al ratio of 0.7 (analysis 12 in Table S4), consistent with the presence of an amorphous (gel) zeolitic precursor.[67,68]The zeolitic phases include significant amounts of PTE: up to 500 ppm Zn, 300 ppm V, and 800 ppm Cu in NaP1; up to 1000 ppm Cu, and 200 ppm As in hydroxysodalite, and up to 600 ppm Cu, 500 ppm Mn, 500 ppm Zn, 3600 ppm Cr and 2400 ppm V in the amorphous zeolitic precursor (Table S4). Very similar results are observed in zeolitic products of run K1 (Fig. S5, Table S6), where K zeolite with a representative formula $K_{2.34}Na_{0.62}Mg_{0.68}Ca_{0.11}Fe_{0.22}Al_{3.33}Si_9O_{24} \cdot 7H_2O$ (analysis #5, Table S5) is identified. The newly formed K zeolite includes significant amounts of PTE: e.g., up to 424 ppm V, up to 631 Cr and up to 406 Mn. In the case of the bicarbonate runs, TEM-SAED reveals the presence of aggregates made up of amorphous nanoparticles ~20-50 nm in size attached to the CFA spheres (Fig. S6). AEM analysis shows that in N2 runs they have a formula $Na_{3.56}K_{0.47}Ca_{0.74}Al_{5.97}Si_{10}O_{32} \cdot 12H_2O$ (analysis #3, Table S6), consistent with the formation of a (NaP1) zeolitic precursor. Similar nanosized amorphous zeolitic precursors have been observed previously.[68,69] Interestingly, EDS mapping and AEM point analyses of CFA spheres in this same run show Na-enrichment (up to 2 wt% Na_2O; analysis #2 in Table S6), which points to formation of zeolitic precursors blanketing the sphere. A relative high concentration of PTE such as Cu, V, and Mn is present in the reacted CFA spheres (Table S6). Altogether, these TEM-AEM results demonstrate that PTE originally present in CFA are preferentially incorporated into the newly-formed amorphous zeolitic precursor and zeolite

phases.

Finally, Brunauer-Emmett-Telller (BET) analysis[70] shows that the unreacted CFA and the control A1 have a surface area of 1.1±0.1 m^2g^{-1}, whereas N1, K1, N2 and K2 have a surface area of 20.4±0.7 m^2g^{-1}, 4.3±0.1 m^2g^{-1}, 2.1±0.1 m^2g^{-1}, and 1.2±0.1 m^2g^{-1}, respectively. These results show that the formation of zeolites in N1 and K1 runs significantly increases the surface area, as expected for the presence of such microporous solids. They also show that the best absorbent product is achieved using Na_2CO_3 as alkaline activator. Interestingly, in the case of run N2, the surface area increases ~100% as compared with unreacted CFA. This is consistent with the formation of the amorphous zeolitic precursor detected with TEM, which reportedly are nanosized and have a relatively high surface area.[56] Following zeolite formation in run K1 and, specially, in run N1, the isotherm of CFA changes from type II (typical of non-porous solids) to a combination of type II and type IV with H4 hysteresis loop typical of micro/mesoporous solids (Fig. S7).[70] The hysteresis loop is not that well defined in run N2, is nearly absent in run K1, and is completely absent in the unreacted CFA and control run A1. The latter further confirms that a zeolitic precursor is formed in the former runs, particularly in run N2.

Factors affecting the progress of carbonation. The higher carbonation reached in carbonate solutions (K1, N1) as compared to bicarbonate solutions (K2, N2) can be explained considering the much higher initial pH of the former solutions.[71] CFA dissolution is significantly pH-dependent, increasing the dissolution rate with increasing pH[9,18–22,72–74]. This is similar to the solubility trend of amorphous silica, which increases sharply for pH >9.0.[62] Since Ca (and Mg)

must be free in solution to be available for carbonation, an increase in pH should result in an increase in the amount of (Mg)calcite formed.[75] Moreover, at pH>10.3, the dominant C species in solution is CO_3^{2-} which is the species involved in the formation of carbonates, whereas at pH<10.3, HCO_3^- is the main aqueous C species, this limiting the extent of carbonation.

The lower CE of K1 run as compared with N1 run cannot be associated with a pH effect, because the initial (and final) pH of the former run was higher that the latter one (Table 1). The Ca concentration in solution (and also Si and Al, see Fig. S8) was significantly higher in K_2CO_3 than in Na_2CO_3 experiments, although not much difference was observed in bicarbonate experiments. This fact shows that the presence of Na^+ ions enhances the formation of crystalline phases acting as "structure builders", whereas K^+ ions hamper the precipitation of secondary phases, in agreement with Monasterio-Guillot et al[62]. Because Na^+ favours the precipitation of secondary crystalline phases (carbonates and zeolites), a more thorough dissolution of the amorphous Ca- and Mg-containing aluminosilicate spheres occurs, shifting the reaction towards the product side and fully explaining the contrasting results of N1 and K1 runs.

Factors affecting zeolite formation. Our results show that: (i) a wider variety of zeolites are formed in the presence of Na^+ as compared to K^+, under otherwise similar experimental conditions, and (ii) higher zeolite yields are obtained with Na^+ as background ion, in agreement with Zeng et al.[42] Crystalline zeolites were not detected in bicarbonate solutions, or in the controls with just water. Murayama et al.[20] showed that the presence of high OH^- concentration in solution contributes to the release of Si and Al from CFA and, above 120ºC,

allows the formation of an aluminosilicate gel, which is the precursor of zeolites. In our work, zeolites form due to a combination of the hydrothermal conditions (T >120ºC) and the alkaline pH (>10)[9,18–22,25,72–74]. The release of Al and Si during dissolution of the CFA occurs in different stages, initially beginning with the dissolution of the glass, which is the most reactive phase, followed by quartz and mullite.[19] Commonly, high concentrations of NaOH or KOH (typically 1 to 5 M) under hydrothermal conditions (>120ºC) have been used to promote the dissolution of the glass fraction and the subsequent precipitation of zeolite-type phases.[8,18,20–22,42,72,76] Interestingly, the high zeolite yield observed in the presence of Na^+ ions in run N1, which also yields the maximum amount of calcium carbonate, suggests that a synergistic action is at work during the precipitation of these phases. Apparently, higher levels of dissolution of the amorphous aluminosilicates in CFA are favored by the joint formation of both carbonates and zeolites, enabling a higher conversion of CFA into crystalline product phases. Remarkably, the high zeolite yield observed here is achieved at relatively mild T conditions with sodium carbonate solutions with lower $[OH]^-$ concentrations than typically used for zeolite synthesis via NaOH alkaline activation. Moreover, our route does not require alkali-fusion of CFA at high T (>500 °C), or the use of energy intensive microwave synthesis[25], which is advantageous from an economic and environmental point of view.

Toxic elements leaching. Unreacted CFA shows a general higher release of PTE to the solution at both near-neutral and alkaline pHs as compared to reacted samples (Fig. 4). This effect is most marked in runs N1 and K1, although solids from run N2 and K2 also show a

significant reduction in PTE release. The release of As is pH-dependent for unreacted CFA, being higher at pH 6 than at pH 10. It has been reported that alkaline CFAs, like the one used here, show higher As release rates at high pH than at low pH, whereas the opposite is true for acidic CFA.[77] Release of As from unreacted CFA is eight times higher than in reacted CFA. Such a huge difference is ascribed to its adsorption/entrapment into newly formed zeolites (or zeolite precursors in bicarbonate runs). The behaviour of V and Sb (Figure S4c and f) is very similar to that of As[78], yet some subtle differences are observed. For instance, unreacted CFA present a higher Sb release at near neutral pH than at alkaline pH, whereas reacted samples show the opposite behaviour. This is likely due to the incorporation of this element in non-silicate phases (iron oxides) which prevent its release at acid-neutral pH, but is solubilized at alkaline pH.[77] Regarding heavy metal ions such as Cu, Mo and Zn (as well as Sr, Mn and Ni) we observe that their release rate is strongly pH-dependent (Fig. 4). At alkaline pH a systematic reduction in release rate occurs in reacted CFA as compared to unreacted CFA. This is consistent with the trapping of these metals both in carbonate and zeolitic phases as shown by our TEM-AEM and SEM-EDS. In the case of Cu, this is likely due to its incorporation into zeolites as nanophase $Cu(OH)_2$ or CuO, as demonstrated by Terzano et al.[79] In contrast, at pH 6 all these elements tend to be released at a higher rate in reacted than in unreacted CFA samples. A likely explanation for this behaviour is the release of such metals from their calcite host after the proton-promoted dissolution of the latter phase. Altogether, our results show that the precipitation of secondary phases plays a key role in the immobilization of PTE. Our leaching

results show that at alkaline conditions (i.e., the natural pH of this alkaline CFA), the PTE release of reacted samples including zeolitic precursors, zeolites and calcite, is significantly reduced as compared with raw CFA (i.e. As leaching in unreacted material (80 ppb) while in K2 run (1.9 ppb) in pH 6; V leaching in unreacted material 80 ppb, while in N2 run 30 ppb). However, at mildly acidic conditions, release of some specific PTE trapped in newly formed carbonates might be an issue. Nonetheless, because after carbonation/zeolitization the pH of the CFA remains alkaline, such an acid-promoted PTE release will be unlikely if, for instance, the reacted CFA is disposed of in a pond or landfilled. Although CFA has been shown to be able to adsorb different acid gasses, including CO_2, and different PTE and organic pollutant, such an adsorption is known to be very poor.[80] Transformation of CFA into carbonates and zeolites can overcome such limitations as it is shown here.

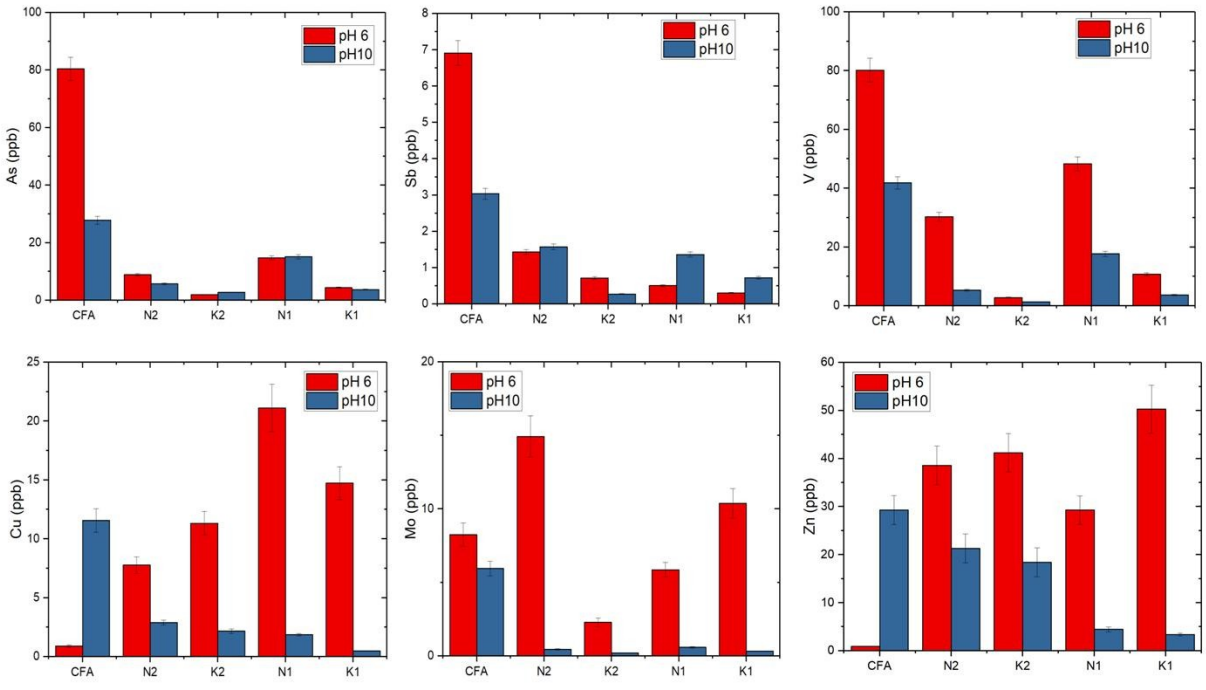

Figure 4. Results of leaching tests performed at pH 6 and pH 10. The total amount of selected

elements (As, Sb, V, Cu, Mo, and Zn) leached from the unreacted CFA as well as of product from runs N2, K2, Ni and K1 is presented. The total amount was calculated by integrating the amount of element released at the predetermined sampling time intervals indicated in Materials and Methods.

Implications. We demonstrate that 1 ton of CFA can contribute to the sequestration of 45 kg of CO_2, a value that is much higher than those reported for other CFA, even with higher CaO (and MgO) contents.[28,81–83] Still, this capacity is relatively small if compared with other alkaline waste materials such as steel slag, cement kiln dust, municipal solid waste incinerator (MSWI) ash or air pollution control (APC) residues where values of net CO_2 mineral sequestration up to 290 kg of CO_2/ton of alkaline waste have been reported.[35] However, considering the amount of CFA produced annually worldwide, and the amount already landfilled, CFA carbonation can effectively contribute to the reduction of the C footprint of the coal-firing sector.

We also show that the background alkaline metal ion plays a key role in the carbonation and zeolitization efficiency. The "structure builder" role of Na^+, led to 60 wt% conversion of CFA into zeolites, also reaching the highest CE of all runs (79.26 %). To our knowledge, these values are among the highest ones obtained for zeolite conversion and carbonation efficiency using CFA.[18,19,52,73] In contrast, with K^+ as background electrolyte, only a 30% zeolitic yield and about half the CE of the N1 run were achieved. These results demonstrate that the use of a sodium alkaline solution for CO_2 mineral capture and zeolite production is the best choice.

Finally, what is more important is that CFA carbonation/zeolitization makes less

460 hazardous these wastes for their disposal of in ponds or landfills, while simultaneously
461 increasing their value as a result of the formation of reaction byproducts (carbonates and
462 zeolites) with a potential commercial use in several applications, with promising capacities to
463 immobilize PTE from wastewaters, or for flue gas treatment and separation of different
464 greenhouse gases (e.g., CO_2, NH_4). Ultimately, our study opens a new pathway on the combined
465 carbonation and zeolitisation of CFA under hydrothermal conditions to add an extra value to
466 these wastes to form reusable materials and, also, to avoid the hazardous consequences due to
467 the leaching of potentially toxic elements.
468
469 **Acknowledgement:** This research has been funded by the Spanish Government (grant
470 RTI2018-099565-B-I00), European Commission (ERDF funds), the Junta de Andalucía
471 (research group RNM-179), and the University of Granada (Unidad Científica de Excelencia
472 UCE-PP2016-05). TGA-DSC analyses were partially funded by a grant from Labex
473 OSUG@2020 (investissements d'avenir, ANR10-LABX56). Use of the Analytical Chemistry
474 platform of ISTerre is acknowledged. LMG acknowledges funding by the Spanish Government
475 (Grant BES-2016-078468). We thank the personnel of the Centro de Instrumentación Científica
476 (CIC; University of Granada) for assistance with ICP-OES, ICP-MS, FESEM and TEM
477 analyses. We also thank M. Burgos for his help with N_2 sorption analyses.
478
479 **References**
480 (1) IPCC. *Climate Change 2014: Synthesis Report. Fifth Assesment Report of the*

Intergovernmental Panel on Climate Change; 2014. https://doi.org/10.1016/S0022-0248(00)00575-3.

(2) Bhatt, A.; Priyadarshini, S.; Mohanakrishnan, A. A.; Abri, A.; Sattler, M.; Techapaphawit, S. Physical, Chemical, and Geotechnical Properties of Coal Fly Ash: A Global Review. *Case Stud. Constr. Mater.* **2019**, *11*, e00263.

(3) Wee, J. H. A Review on Carbon Dioxide Capture and Storage Technology Using Coal Fly Ash. *Appl. Energy* **2013**, *106*, 143–151. https://doi.org/10.1016/j.apenergy.2013.01.062.

(4) Blissett, R. S.; Rowson, N. A. A Review of the Multi-Component Utilisation of Coal Fly Ash. *Fuel* **2012**, *97*, 1–23.

(5) Ji, L.; Yu, H.; Wang, X.; Grigore, M.; French, D.; Gözükara, Y. M.; Yu, J.; Zeng, M. CO2sequestration by Direct Mineralisation Using Fly Ash from Chinese Shenfu Coal. *Fuel Process. Technol.* **2017**, *156*, 429–437. https://doi.org/10.1016/j.fuproc.2016.10.004.

(6) European Coal Combustion Products Association e.V.

(7) American Coal Ash Association's.

(8) Dwivedi, A.; Jain, M. K. Fly Ash – Waste Management and Overview : A Review. *Recent Res. Sci. Technol.* **2014**, *6* (1), 30–35. https://doi.org/10.1111/j.1523-1739.2008.00978.x.

(9) Querol, X.; Plana, F.; Alastuey, A.; Lbpez-Soler, A. Synthesis of Na-Zeolites from Fly Ash. *Fuel* **1997**, *76* (8), 236100188–3. https://doi.org/10.1016/S0016-2361(96)00188-3.

(10) Álvarez-Ayuso, E.; García-Sánchez, A.; Querol, X. Purification of Metal Electroplating

Waste Waters Using Zeolites. *Water Res.* **2003**, *37* (20), 4855–4862. https://doi.org/10.1016/j.watres.2003.08.009.

(11) Moreno, N.; Querol, X.; Andrés, J. M.; Stanton, K.; Towler, M.; Nugteren, H.; Janssen-Jurkovicová, M.; Jones, R. Physico-Chemical Characteristics of European Pulverized Coal Combustion Fly Ashes. *Fuel* **2005**, *84* (11), 1351–1363.

(12) Ruhl, L.; Vengosh, A.; Dwyer, G. S.; Hsu-Kim, H.; Deonarine, A. Environmental Impacts of the Coal Ash Spill in Kingston, Tennessee: An 18-Month Survey. *Environ. Sci. Technol.* **2010**, *44* (24), 9272–9278.

(13) Catalano, J. G.; Huhmann, B. L.; Luo, Y.; Mitnick, E. H.; Slavney, A.; Giammar, D. E. Metal Release and Speciation Changes during Wet Aging of Coal Fly Ashes. *Environ. Sci. Technol.* **2012**, *46* (21), 11804–11812.

(14) Yang, Y.; Colman, B. P.; Bernhardt, E. S.; Hochella, M. F. Importance of a Nanoscience Approach in the Understanding of Major Aqueous Contamination Scenarios: Case Study from a Recent Coal Ash Spill. *Environ. Sci. Technol.* **2015**, *49* (6), 3375–3382.

(15) Harkness, J. S.; Sulkin, B.; Vengosh, A. Evidence for Coal Ash Ponds Leaking in the Southeastern United States. *Environ. Sci. Technol.* **2016**, *50* (12), 6583–6592.

(16) Brandt, J. E.; Simonin, M.; Di Giulio, R. T.; Bernhardt, E. S. Beyond Selenium: Coal Combustion Residuals Lead to Multielement Enrichment in Receiving Lake Food Webs. *Environ. Sci. Technol.* **2019**, *53* (8), 4119–4127.

(17) Höller, H.; Wirsching, U. Zeolite Formation from Fly Ash. *Fortschritte der Mineral.* **1985**, *63* (1), 21–43.

(18) Lin, C. F.; Hsi, H. C. Resource Recoveiy of Waste Fly Ash: Synthesis of Zeolite-like Materials. *Environ. Sci. Technol.* **1995**, *29* (4), 1109–1117. https://doi.org/10.1021/es00004a033.

(19) Querol, X.; Moreno, N.; Umaa, J. C.; Alastuey, A.; Hernández, E.; López-Soler, A.; Plana, F. Synthesis of Zeolites from Coal Fly Ash: An Overview. *Int. J. Coal Geol.* **2002**, *47* (1–4), 413–423. https://doi.org/10.1088/1757-899X/230/1/012044.

(20) Murayama, N.; Yamamoto, H.; Shibata, J. Mechanism of Zeolite Synthesis from Coal Fly Ash by Alkali Hydrothermal Reaction. *Int. J. Miner. Process.* **2002**, *64* (1), 1–17. https://doi.org/10.1016/S0301-7516(01)00046-1.

(21) Querol, X.; Alastuey, A.; López-Soler, A.; Plana, F.; Andrés, J. M.; Juan, R.; Ferrer, P.; Ruiz, C. R. A Fast Method for Recycling Fly Ash: Microwave-Assisted Zeolite Synthesis. *Environ. Sci. Technol.* **1997**, *31* (9), 2527–2533. https://doi.org/10.1021/es960937t.

(22) Steenbruggen, G.; Hollman, G. G. The Synthesis of Zeolites from Fly Ash and the Properties of the Zeolite Products. *J. Geochemical Explor.* **1998**, *62* (1–3), 305–309. https://doi.org/10.1016/S0375-6742(97)00066-6.

(23) Inglezakis, V. J.; Grigoropoulou, H. P. Applicability of Simplified Models for the Estimation of Ion Exchange Diffusion Coefficients in Zeolites. *J. Colloid Interface Sci.* **2001**, *234* (2), 434–441. https://doi.org/10.1006/jcis.2000.7304.

(24) Singer, A.; Berkgaut, V. Cation Exchange Properties of Hydrothermally Treated Coal Fly Ash. *Environ. Sci. Technol.* **1995**, *29* (7), 1748–1753.

(25) Moreno, N.; Querol, X.; Ayora, C.; Pereira, C. F.; Janssen-Jurkovicová, M. Utilization of Zeolites Synthesized from Coal Fly Ash for the Purification of Acid Mine Waters. *Environ. Sci. Technol.* **2001**, *35* (17), 3526–3534. https://doi.org/10.1021/es0002924.

(26) Lee, K.-M.; Jo, Y.-M. Synthesis of Zeolite from Waste Fly Ash for Adsorption of CO 2. *J. Mater. Cycles Waste Manag.* **2010**, *12* (3), 212–219.

(27) Chang, E. E.; Chen, C. H.; Chen, Y. H.; Pan, S. Y.; Chiang, P. C. Performance Evaluation for Carbonation of Steel-Making Slags in a Slurry Reactor. *J. Hazard. Mater.* **2011**, *186* (1), 558–564. https://doi.org/10.1016/j.jhazmat.2010.11.038.

(28) Tamilselvi Dananjayan, R. R.; Kandasamy, P.; Andimuthu, R. Direct Mineral Carbonation of Coal Fly Ash for CO2sequestration. *J. Clean. Prod.* **2016**. https://doi.org/10.1016/j.jclepro.2015.05.145.

(29) Ecke, H. Sequestration of Metals in Carbonated Municipal Solid Waste Incineration (MSWI) Fly Ash. *Waste Manag.* **2003**, *23* (7), 631–640. https://doi.org/10.1016/S0956-053X(03)00095-3.

(30) Montes-Hernandez, G.; Pérez-López, R.; Renard, F.; Nieto, J. M.; Charlet, L. Mineral Sequestration of CO2 by Aqueous Carbonation of Coal Combustion Fly-Ash. *J. Hazard. Mater.* **2009**, *161* (2–3), 1347–1354. https://doi.org/10.1016/j.jhazmat.2008.04.104.

(31) Thomas, M. D. A.; Matthews, J. D. Carbonation of Fly Ash Concrete. *Mag. Concr. Res.* **1992**, *44* (160), 217–228. https://doi.org/10.1680/macr.1992.44.160.217.

(32) Wang, L.; Jin, Y.; Nie, Y. Investigation of Accelerated and Natural Carbonation of MSWI Fly Ash with a High Content of Ca. *J. Hazard. Mater.* **2010**, *174* (1–3), 334–343.

https://doi.org/10.1016/j.jhazmat.2009.09.055.

(33) Back, M.; Kuehn, M.; Stanjek, H.; Peiffer, S. Reactivity of Alkaline Lignite Fly Ashes towards CO2 in Water. *Environ. Sci. Technol.* **2008**, *42* (12), 4520–4526.

(34) Evangelos Georgakopoulos (Cranfield University, UK), Rafael M. Santos (Sheridan Institute of Technology, Brampton, Ontario, Canada), Yi Wai Chiang (University of Guelph, Ontario, Canada), Vasilije Manovic (Cranfield University, U. Influence of Process Parameters on Carbonation Rate and Conversion of Steelmaking Slags – Introduction of the 'Carbonation Weathering Rate.' *Greenh. Gases Sci. Technol.* **2016**, *6* (4), 470–491. https://doi.org/10.1002/ghg.

(35) Pan, S. Y.; Chang, E. E.; Chiang, P. C. CO2capture by Accelerated Carbonation of Alkaline Wastes: A Review on Its Principles and Applications. *Aerosol Air Qual. Res.* **2012**, *12* (5), 770–791. https://doi.org/10.4209/aaqr.2012.06.0149.

(36) Bauer, M.; Gassen, N.; Stanjek, H.; Peiffer, S. Carbonation of Lignite Fly Ash at Ambient T and P in a Semi-Dry Reaction System for CO2 Sequestration. *Appl. geochemistry* **2011**, *26* (8), 1502–1512.

(37) Ji, L.; Yu, H.; Yu, B.; Zhang, R.; French, D.; Grigore, M.; Wang, X.; Chen, Z.; Zhao, S. Insights into Carbonation Kinetics of Fly Ash from Victorian Lignite for CO 2 Sequestration. **2018**. https://doi.org/10.1021/acs.energyfuels.7b03137.

(38) ICDD. PDF-2. Newtown Square, PA 1996.

(39) Rietveld, H. M. A Profile Refinement Method for Nuclear and Magnetic Structures. *J. Appl. Crystallogr.* **1969**, *2* (2), 65–71. https://doi.org/10.1107/S0021889869006558.

(40) De La Torre, A. G.; Bruque, S.; Aranda, M. A. G. Rietveld Quantitative Amorphous Content Analysis. *J. Appl. Crystallogr.* **2001**, *34* (2), 196–202. https://doi.org/10.1107/S0021889801002485.

(41) Cliff, G.; Lorimer, G. The Quantitative Analysis of Thin Specimens. *J. Microsc.* **1975**, *103* (2), 203–207.

(42) Zeng, R.; Umana, J. C.; Querol, X.; Lopez-Soler, A.; Plana, F.; Zhuang, X. Zeolite Synthesis from a High Si-Al Fly Ash from East China. *J. Chem. Technol. Biotechnol.* **2002**, *77* (3), 267–273. https://doi.org/10.1002/jctb.598.

(43) Monasterio-Guillot, L.; Di Lorenzo, F.; Ruiz-Agudo, E.; Rodriguez-Navarro, C. Reaction of Pseudowollastonite with Carbonate-Bearing Fluids: Implications for CO2 Mineral Sequestration. *Chem. Geol.* **2019**, *524*, 158–173. https://doi.org/10.1016/j.chemgeo.2019.06.011.

(44) Thiery, M.; Villain, G.; Dangla, P.; Platret, G. Investigation of the Carbonation Front Shape on Cementitious Materials: Effects of the Chemical Kinetics. **2007**. https://doi.org/10.1016/j.cemconres.2007.04.002.

(45) Nyambura, M. G.; Mugera, G. W.; Felicia, L.; Gathura, N. P. *Carbonation of Brine Impacted Fractionated Coal Fly Ash: Implications for CO 2 Sequestration*.

(46) Fernández Bertos, M.; Simons, S. J. R.; Hills, C. D.; Carey, P. J. A Review of Accelerated Carbonation Technology in the Treatment of Cement-Based Materials and Sequestration of CO 2. *J. Hazard. Mater.* **2004**, *112*, 193–205. https://doi.org/10.1016/j.jhazmat.2004.04.019.

(47) Duxson, P.; Provis, J. L. Designing Precursors for Geopolymer Cements. *J. Am. Ceram. Soc.* **2008**, *91* (12), 3864–3869.

(48) Vassilev, S. V; Menendez, R.; Alvarez, D.; Diaz-Somoano, M.; Martinez-Tarazona, M. R. Phase-Mineral and Chemical Composition of Coal Fly Ashes as a Basis for Their Multicomponent Utilization. 1. Characterization of Feed Coals and Fly Ashes☆. *Fuel* **2003**, *82* (14), 1793–1811.

(49) Farmer, V. C. Orthosilicates, Pyrosilicates, and Other Finite-Chain Silicates. In *The Infrared Spectra of Minerals*; Farmer, V. C., Ed.; Mineralogical Society of Great Britain and Ireland, 1974.

(50) Mozgawa, W.; Mozgawa, W.; Handke, M.; Jastrze, W. Vibrational Spectra of Aluminosilicate Structural Clusters Synthesis and Structural Studies of Zeolite Membranes on Geopolimeric Supports View Project Vibrational Spectra of Aluminosilicate Structural Clusters. *Artic. J. Mol. Struct.* **2004**. https://doi.org/10.1016/j.molstruc.2004.01.059.

(51) Fernández−Pereira, C.; Galiano, Y. L.; Rodríguez−Piñero, M. A.; Vale, J.; Querol, X. Utilisation of Zeolitised Coal Fly Ash as Immobilising Agent of a Metallurgical Waste. *J. Chem. Technol. Biotechnol. Int. Res. Process. Environ. Clean Technol.* **2002**, *77* (3), 305–310.

(52) Sánchez-Hernández, R.; López-Delgado, A.; Padilla, I.; Galindo, R.; López-Andrés, S. One-Step Synthesis of NaP1, SOD and ANA from a Hazardous Aluminum Solid Waste. *Microporous Mesoporous Mater.* **2016**, *226*, 267–277.

(53) Kosanovic, C.; Subotic, B.; Smit, I.; Cizmek, A.; Stubicar, M.; Tonejc, A. Study of Structural Transformations in Potassium-Exchanged Zeolite A Induced by Thermal and Mechanochemical Treatments. *J. Mater. Sci.* **1997**, *32* (1), 73–78.

(54) Fahlke, B.; Starke, P.; Seefeld, V.; Wieker, W.; Wendlandt, K.-P. On the Intermediates in Zeolite Y Synthesis. *Zeolites* **1987**, *7* (3), 209–213.

(55) Shigemoto, N.; Sugiyama, S.; Hayashi, H.; Miyaura, K. Characterization of Na-X, Na-A, and Coal Fly Ash Zeolites and Their Amorphous Precursors by IR, MAS NMR and XPS. *J. Mater. Sci.* **1995**, *30* (22), 5777–5783.

(56) Morsli, A.; Driole, M.-F.; Cacciaguerra, T.; Arletti, R.; Chiche, B.; Hamidi, F.; Bengueddach, A.; Quignard, F.; Di Renzo, F. Microporosity of the Amorphous Aluminosilicate Precursors of Zeolites: The Case of the Gels of Synthesis of Mordenite. *Microporous mesoporous Mater.* **2007**, *104* (1–3), 209–216.

(57) rodriguez-Navarro, C.; ruiz-agudo, eNCarNaCioN; luque, aNa; rodriguez-Navarro, alejaNdro B.; ortega-Huertas, M. Thermal Decomposition of Calcite: Mechanisms of Formation and Textural Evolution of CaO Nanocrystals. *Am. Mineral.* **2009**, *94*, 578–593. https://doi.org/10.2138/am.2009.3021.

(58) Demir, F.; Dönmez, B.; Okur, H.; Sevim, F. Calcination Kinetic of Magnesite from Thermogravimetric Data. *Chem. Eng. Res. Des.* **2003**, *81* (6), 618–622.

(59) de Souza, F.; Bragança, S. R. Thermogravimetric Analysis of Limestones with Different Contents of MgO and Microstructural Characterization in Oxy-Combustion. *Thermochim. Acta* **2013**, *561*, 19–25.

(60) Goldsmith, J. R.; Graf, D. L.; Chodos, A. A.; Joensuu, O. I.; McVicker, L. D. Relation between Lattice Constants and Composition of Ca-Mg Carbonates. *Am. Mineral. J. Earth Planet. Mater.* **1958**, *43* (1–2), 84–101.

(61) Mavromatis, V.; Gautier, Q.; Bosc, O.; Schott, J. Kinetics of Mg Partition and Mg Stable Isotope Fractionation during Its Incorporation in Calcite. *Geochim. Cosmochim. Acta* **2013**, *114*, 188–203.

(62) Monasterio-Guillot, L.; Di Lorenzo, F.; Ruiz-Agudo, E.; Rodriguez-Navarro, C. Reaction of Pseudowollastonite with Carbonate-Bearing Fluids: Implications for CO<inf>2</Inf> Mineral Sequestration. *Chem. Geol.* **2019**, *524*. https://doi.org/10.1016/j.chemgeo.2019.06.011.

(63) Casey, W. H.; Westrich, H. R.; Massis, T.; Banfield, J. F.; Arnold, G. W. The Surface of Labradorite Feldspar after Acid Hydrolysis. *Chem. Geol.* **1989**, *78* (3–4), 205–218. https://doi.org/10.1016/0009-2541(89)90058-2.

(64) Hellmann, R.; Penisson, J. M.; Hervig, R. L.; Thomassin, J. H.; Abrioux, M. F. An EFTEM/HRTEM High-Resolution Study of the near Surface of Labradorite Feldspar Altered at Acid PH: Evidence for Interfacial Dissolution-Reprecipitation. *Phys. Chem. Miner.* **2003**, *30* (4), 192–197. https://doi.org/10.1007/s00269-003-0308-4.

(65) Ruiz-Agudo, E.; King, H. E.; Patiño-López, L. D.; Putnis, C. V; Geisler, T.; Rodriguez-Navarro, C.; Putnis, A. Control of Silicate Weathering by Interface-Coupled Dissolution-Precipitation Processes at the Mineral-Solution Interface. *Geol.* **2016**, *44* (7), 1–4. https://doi.org/10.1130/G37856.1.

(66) Ruiz-Agudo, E.; Putnis, C. V.; Rodriguez-Navarro, C.; Putnis, A. Mechanism of Leached Layer Formation during Chemical Weathering of Silicate Minerals. *Geology* **2012**, *40* (10), 947–950. https://doi.org/10.1130/G33339.1.

(67) Catalfamo, P.; Corigliano, F.; Primerano, P.; Di Pasquale, S. Study of the Pre-Crystallization Stage of Hydrothermally Treated Amorphous Aluminosilicates through the Composition of the Aqueous Phase. *J. Chem. Soc. Faraday Trans.* **1993**, *89* (1), 171–175.

(68) Itani, L.; Liu, Y.; Zhang, W.; Bozhilov, K. N.; Delmotte, L.; Valtchev, V. Investigation of the Physicochemical Changes Preceding Zeolite Nucleation in a Sodium-Rich Aluminosilicate Gel. *J. Am. Chem. Soc.* **2009**, *131* (29), 10127–10139.

(69) Yan, F.; Jiang, J.; Li, K.; Tian, S.; Zhao, M.; Chen, X. Performance of Coal Fly Ash Stabilized, CaO-Based Sorbents under Different Carbonation−Calcination Conditions. **2015**. https://doi.org/10.1021/acssuschemeng.5b00355.

(70) Thommes, M.; Kaneko, K.; Neimark, A. V; Olivier, J. P.; Rodriguez-Reinoso, F.; Rouquerol, J.; Sing, K. S. W. Physisorption of Gases, with Special Reference to the Evaluation of Surface Area and Pore Size Distribution (IUPAC Technical Report). *Pure Appl. Chem.* **2015**, *87* (9–10), 1051–1069.

(71) Parkhurst, D. L.; Appelo, C. A. J. *USER'S GUIDE TO PHREEQC (VERSION 2)-A COMPUTER PROGRAM FOR SPECIATION, BATCH-REACTION, ONE-DIMENSIONAL TRANSPORT, AND INVERSE GEOCHEMICAL CALCULATIONS*.

(72) Shigemoto, N.; Hayashi, H.; Miyaura, K. Selective Formation of Na-X Zeolite from Coal

Fly Ash by Fusion with Sodium Hydroxide Prior to Hydrothermal Reaction. *J. Mater. Sci.* **1993**, *28* (17), 4781–4786. https://doi.org/10.1007/BF00414272.

(73) Hollman, G. G.; Steenbruggen, G.; Janssen-Jurkovičová, M. Two-Step Process for the Synthesis of Zeolites from Coal Fly Ash. *Fuel* **1999**, *78* (10), 1225–1230. https://doi.org/10.1016/S0016-2361(99)00030-7.

(74) Du Plessis, P. W.; Ojumu, T. V.; Petrik, L. F. Waste Minimization Protocols for the Process of Synthesizing Zeolites from South African Coal Fly Ash. *Materials (Basel).* **2013**, *6* (5), 1688–1703. https://doi.org/10.3390/ma6051688.

(75) Rodríguez-Navarro, C.; Ruiz-Agudo, E.; Harris, J.; Wolf, S. E. Nonclassical Crystallization in Vivo et in Vitro (II): Nanogranular Features in Biomimetic Minerals Disclose a General Colloid-Mediated Crystal Growth Mechanism. **2016**. https://doi.org/10.1016/j.jsb.2016.09.005.

(76) Henry, J.; Towler, M. R.; Stanton, K. T.; Querol, X.; Moreno, N. Characterisation of the Glass Fraction of a Selection of European Coal Fly Ashes. *J. Chem. Technol. Biotechnol.* **2004**, *79* (5), 540–546. https://doi.org/10.1002/jctb.1023.

(77) Izquierdo, M.; Querol, X. Leaching Behaviour of Elements from Coal Combustion Fly Ash: An Overview. *Int. J. Coal Geol.* **2012**, *94*, 54–66. https://doi.org/10.1016/j.coal.2011.10.006.

(78) Spears, D. A.; Martinez-Tarrazona, M. R. Trace Elements in Combustion Residues from a UK Power Station. *Fuel* **2004**, *83* (17–18), 2265–2270.

(79) Terzano, R.; Spagnuolo, M.; Medici, L.; Vekemans, B.; Vincze, L.; Janssens, K.;

712 Ruggiero, P. Copper Stabilization by Zeolite Synthesis in Polluted Soils Treated with
713 Coal Fly Ash. *Environ. Sci. Technol.* **2005**, *39* (16), 6280–6287.
714 https://doi.org/10.1021/es050079d.
715 (80) Gupta, V. K.; Carrott, P. J. M.; Ribeiro Carrott, M. M. L.; Suhas. Low-Cost Adsorbents:
716 Growing Approach to Wastewater Treatment—a Review. *Crit. Rev. Environ. Sci.*
717 *Technol.* **2009**, *39* (10), 783–842.
718 (81) Ukwattage, N. L.; Ranjith, P. G.; Yellishetty, M.; Bui, H. H.; Xu, T. A Laboratory-Scale
719 Study of the Aqueous Mineral Carbonation of Coal Fly Ash for CO2 Sequestration. *J.*
720 *Clean. Prod.* **2015**, *103*, 665–674.
721 (82) Sun, Y.; Parikh, V.; Zhang, L. Sequestration of Carbon Dioxide by Indirect
722 Mineralization Using Victorian Brown Coal Fly Ash. *J. Hazard. Mater.* **2012**, *209–210*,
723 458–466. https://doi.org/10.1016/j.jhazmat.2012.01.053.
724 (83) He, L.; Yu, D.; Lv, W.; Wu, J.; Xu, M. A Novel Method for CO 2 Sequestration via
725 Indirect Carbonation of Coal Fly Ash. **2013**. https://doi.org/10.1021/ie4023644.
726